

# Generation of a uniform-square focal spot by a compound lens for solar concentration applications

Shih-Hsin Ma,<sup>1,\*</sup> Chun-Ming Tseng,<sup>1</sup> and Yun-Parn Lee<sup>2</sup>

<sup>1</sup>Department of Photonics, Feng Chia University, No. 100 Wenhward, Seatwen, Taichung City 40724, Taiwan

<sup>2</sup>Department of Electronic Engineering, Ming Chuan University, No. 5 De Ming Road, Gui Shan District, Taoyuan County 33348, Taiwan

\*Corresponding author: shma@fcu.edu.tw

Received 3 January 2013; revised 3 April 2013; accepted 3 April 2013;  
posted 3 April 2013 (Doc. ID 182705); published 26 April 2013

This paper describes a compound lens for solar photovoltaic system applications, which is composed of a front aspheric or Fresnel surface and a back array of concave surfaces. In contrast to earlier designs, the proposed method can simultaneously focus and shape sun light into a uniform-square pattern on the solar cell. For a square solar cell, this approach can maximize the solar cell's opto-electric conversion efficiency by enhancing the concentrated pattern's uniformity. In this article, the theoretical models of the beam shaping focused lens is derived and then compared with experimental data. The tolerance in assembling the component of the concentrator is also analyzed and the corresponding simulation and experimental results are discussed in detail. © 2013 Optical Society of America

*OCIS codes:* (080.4298) Nonimaging optics; (220.4298) Nonimaging optics; (220.2740) Geometric optical design; (220.1770) Concentrators.

<http://dx.doi.org/10.1364/AO.52.003058>

## 1. Introduction

In the past 30 years, due to the continuously growing requirement for solar energy and the development of photovoltaic cells, there are many papers proposing various methods for enhancing solar collection efficiency [1–8]. Among the used optical shapes, the two stage mirrors reflective configuration [9–14] and the multiple-lens refractive configuration [15–17] have been widely utilized to improve collection efficiency and decrease the amount of expensive cells. The photovoltaic cells are usually available only in rectangular shapes due to fabrication and packaging simplicity. Besides, the rectangle shape can cover wide areas without leaving gaps in cutting chips. However, the solar concentrators [Fig. 1(a)] research mostly concentrates on the optical shapes to generate a small

circular spot on the photovoltaic cell and there is a lack of study about the full utilization of the square shape of a photovoltaic cell [Fig. 1(b)].

To further enhance the area utilization efficiency of the square photovoltaic cell, it is necessary to generate a uniform and square light pattern by adopting a solar focused lens with a square-beam shaping ability. The highly uniform-square focal spot usually can be obtained by roughing the segment of compound parabolic concentrator light pipe, which has a square exit pupil or a free-form Köhler concentrator [18,19]. However, the optical efficiency and uniformity of the focal spot easily suffers from the rough surface or the misalignment among multiple optical elements in a solar concentration system. Hence, this paper proposes a single lens, which comprises a front aspheric focusing surface and a back array of concave surfaces. In addition, to decrease the weight and thickness of the lens, a similar design using a front Fresnel profile [20–24] instead of a front aspheric surface is also designed and

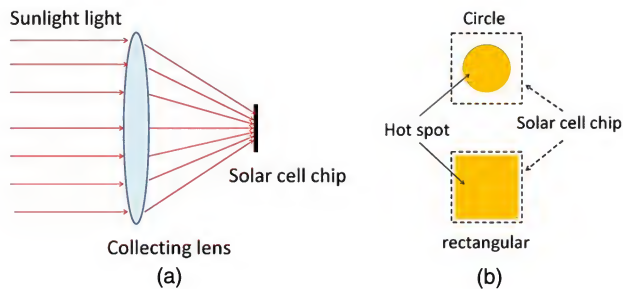


Fig. 1. (a) Simple schematic of a solar concentrator, which consists of a collection lens and a solar cell chip. (b) Collected sunlight is usually focused to a circular spot instead of a rectangular one.

analyzed. The characteristics and experimental data compared with the theoretical calculation will be discussed.

## 2. Design of the Module

Beam shaping is the process of redistributing the phase and irradiance of a beam. A square beam cross section is widely used in laser/material processing [25–35], but less applied in a solar concentrator. Ryu *et al.* [36] first proposed solar concentration optics utilizing a modularly faced Fresnel lens to achieve a square focal spot. Its modularly Fresnel facets generate a collection efficiency larger than 70%, but this complex structure is more difficult in fabrication. Our beam shaping focused lens (BSFL) consists of an aspheric focusing surface (first surface) and a two-dimensional array of concave shaping surfaces (second surface). In the second surface, the exit pupil of each concave surface is square. The schematic layout in the perpendicular direction ( $y$ - $z$  plane) is shown in Fig. 2(a) with all pertinent parameters indicated. Based on the designed concentration ratio, the lens has an entrance edge  $D = 6$  cm, the curvature radius of the first surface  $R = 3.11$  cm, the thickness  $t = 2$  cm, and the back focal length before adding the periodic concave surface  $BFL = 4$  cm. The front surface is modified to an aspheric one for eliminating spherical aberration before adding the periodic concave surfaces. The

aspheric surface of rotation is represented by an equation of the form [37]

$$Z = \frac{cr_a^2}{1 + [1 - c(1 + k)r_a^2]^{\frac{1}{2}}} + a_d r_a^4 + a_e r_a^6 + a_f r_a^8 + a_g r_a^{10} + \dots, \quad (1)$$

where  $Z$  is the sag of the aspheric surface,  $r_a$  the height from the optical axis,  $c$  the curvature,  $k$  the conic constant, and  $a_d$ ,  $a_e$ ,  $a_f$ , and  $a_g$  the high-order coefficients to represent deformations to the spherical surface. The first term of the right side is the equation for a spherical surface of radius  $R = 1/c$  when  $k = 0$ .

Since the uniformity and spot size are related to the radius and diameter of the periodic concave surface, an exit pupil is set to each concave surface in the design. For each concave surface, the first-order angles of the upper rim, the chief and the lower rim rays with respect to the optical axis are  $U_{m1}$ ,  $U_c$ , and  $U_{m2}$ , respectively. If the current concave surface is the  $p$ th one above the optical axis, these angles are given by

$$\text{Upper rim ray: } U_{m1} = \frac{pd}{BFL \cdot n}. \quad (2)$$

$$\text{Chief ray: } U_c = \frac{(p-1)d + d/2}{BFL \cdot n}. \quad (3)$$

$$\text{Lower rim ray: } U_{m2} = \frac{(p-1)d}{BFL \cdot n}. \quad (4)$$

For each concave surface, the incident angles at the vertex plane [Fig. 2(b)]

$$\text{Upper rim ray: } U'_{m1} = -\frac{d}{2r} + \frac{pd}{BFL \cdot n}. \quad (5)$$

$$\text{Chief ray: } U'_c = \frac{(p-1)d + d/2}{BFL \cdot n}. \quad (6)$$

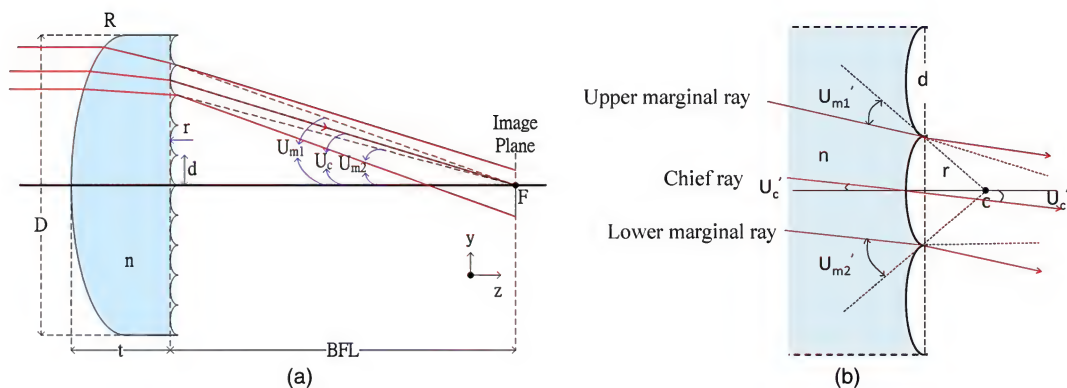


Fig. 2. (a) Schematic sketch of BSFL to illustrate the relationship among the aspheric front surface, the periodic concave surface, and the image plane, where the solar cell is positioned. (b) Relative locations of the refracted rays from the front aspheric surface and the concave surface normals.

$$\text{Lower rim ray: } U'_{m2} = \frac{d}{2r} + \frac{(p-1)d}{\text{BFL} \cdot n}. \quad (7)$$

From the bending equation, the ray angles after the concave surface are given by

$$\text{Upper rim ray: } U''_{m1} = \frac{d}{2r} - n \left( -\frac{d}{2r} + \frac{pd}{\text{BFL} \cdot n} \right). \quad (8)$$

$$\text{Chief ray: } U''_c = n \left( \frac{(p-1)d + d/2}{\text{BFL} \cdot n} \right). \quad (9)$$

$$\text{Lower rim ray: } U''_{m2} = \frac{-d}{2r} + n \left( \frac{d}{2r} + \frac{(p-1)d}{\text{BFL} \cdot n} \right). \quad (10)$$

Next, using the transfer equation, the rays' heights on the image plane can be obtained by

$$\text{Upper rim ray: } y_{\max} = pd - \text{BFL} \times U''_{m1}. \quad (11)$$

$$\text{Chief ray: } y_c = (p - d/2) - \text{BFL} \times U''_c = 0. \quad (12)$$

$$\text{Lower rim ray: } y_{\min} = (p - 1)d - \text{BFL} \times U''_{m2}. \quad (13)$$

The average ray height of the upper rim rays from each concave surface along the  $y$  direction,  $y_{\text{ave}}$ , is set as the half-edge of the chip,  $s/2$ , which is also equal to the average value of the lower rim rays due to symmetry of BSFL. Considering the fabrication ability, the size of each concave surface is set 6 mm  $\times$  6 mm in this case. For a 6 cm incident square collimated beam, the overall concave surface number in the array is 10  $\times$  10. In the starting design,  $s/2$  is set to be 1.5 mm. After substituting these known values into Eqs. (2)–(13), we build a merit function to evaluate the optical performance of BSFL. The variables include  $R$  and aspheric coefficients of the front surface and the radius  $r$  of each concave surface. The target is to achieve a high collection efficiency (>80%) with an acceptable uniformity, a higher transmission efficiency (>85%), and a concentration ratio (>300 $\times$ ) inside the solar chip. These related glossaries are defined as the following:

TE: the optical transmission efficiency, which is defined as the ratio between the incident beam power and the output beam power from the BFSFL system.

CE: the optical collecting efficiency, which is defined as the ratio between the incident beam power and the projected power on the solar cell.

CR: the concentration ratio, which is defined as the ratio between the area of entry pupil and the area of solar cell.

U: the irradiance uniformity, which is defined as the ratio between average and minimum irradiance at the solar cell, or

$$U = \frac{E_{\min}}{E_{\text{avg}}}, \quad (14)$$

where  $E_{\min}$  and  $E_{\text{avg}}$  are the minimum and average irradiance levels, respectively.

One of the promising solutions is obtained as  $r = 7$  cm and  $R = 3.11$  cm. In this case, the square spot formed by overlapping the 10  $\times$  10 square light patterns on the image plane, the solar cell has a transmission efficiency of 91%, a collection efficiency of 84% with a uniformity of 22.55%, and a concentration ratio 314 $\times$ .

Unlike a general imaging homogenizer that uses two square-lens arrays [38–41], our design only adopts one square-lens array for simplifying the system structure, and enhancing the optical transmission efficiency. The cost of adopting such a simple structure is that the light patterns projected by the outer square concave surfaces would be distorted and extended due to their larger slanting incident angles. The distorted pattern however, can overlap with the other opposite distorted patterns from the concave surface at the opposite side (on the  $x$ - $y$  plane) to generate a uniform pattern. Then a uniform-square focal spot can be captured by the square solar cell with weak stray rays around the outside. A further simulation shows that an aspheric concave surface in the array can further improve the pattern uniformity. However, we didn't adopt the aspheric design considering the fabrication complexity and cost.

The final optical configuration simulated by ZEMAX software is shown in Fig. 3(a). ASAP software is then used to obtain the efficiency data [Fig. 3(b)]. The final specification of BSFL is summarized in Table 1. The irradiance distribution and its cross-section along the  $x$  axis are shown in Figs. 4(a) and 4(b), respectively. In Fig. 4(a), the red square frame represents the location of the solar cell, and the white part is the light pattern at the focal point. The chip size is initially designed to be 3 mm  $\times$  3 mm, of which the edge corresponds the 21% of the maximum of the normalized irradiance. In determining U values, 100 sampling points are selected within the measurement region. As illustrated in Fig. 5, we read one value per 0.2 mm  $\times$  0.2 mm for a 2 mm  $\times$  2 mm measurement region.

Fresnel lens function is similar to the conventional lens by refracting the rays and focusing them at one focal point. Considering the lighter and the thinner characteristics of the Fresnel lens, our design is also realized in a Fresnel type (F-BSFL, Fig. 6) by modifying the front aspheric surface into a Fresnel facet, which is an approximation of the curvature of aspheric surface. The irradiance distribution and its cross-section along  $x$  axis are shown in Figs. 7(a) and 7(b), respectively. In Fig. 7(a), the red square frame represents the location of the solar cell, and the white part



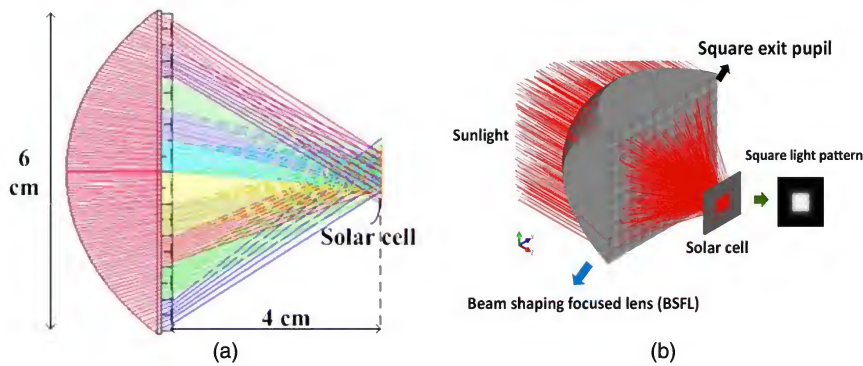


Fig. 3. (a) Initial layout, including the high-order aspheric coefficients, drawn by ZEMAX software. (b) 3D layout and rays distribution simulated by ASAP software. A square light pattern on the solar cell can be observed.

Table 1. Specification of BSFL

Symbol	Description	Value (unit)
$n$	Refractive index of material	1.58
$R$	Curvature radius of the front surface	3.11 cm
$t$	Thickness of the lens	2 cm
BFL	Back focal length before adding the periodic concave surfaces	4 cm
$D$	Diameter of BSFL	6 cm
$d$	Pitch of a concave surface	0.6 cm
$r$	Curvature radius of the back periodic concave surface	7 cm
$N$	Number of the array of concave surfaces	$10 \times 10$

is the light pattern at the focal point. The chip size is also initially designed to be  $3 \text{ mm} \times 3 \text{ mm}$ , of which the edge corresponds to the 30% of the maximum of the normalized irradiance. The optical performances of BSFL and F-BSFL are summarized in Table 2. Compared with a general imaging homogenizer that uses two square-lens arrays, our design has a lower uniformity because light patterns from the outer square concave surfaces [Fig. 8(a)] are more easily distorted and extended than those from the inner [Fig. 8(b)] on the image plane, the solar cell.

In general, the required chip size for BSFL is smaller than that for F-BSFL, TE, CR, and U but CE values are lower in BSFL. The cause is mainly

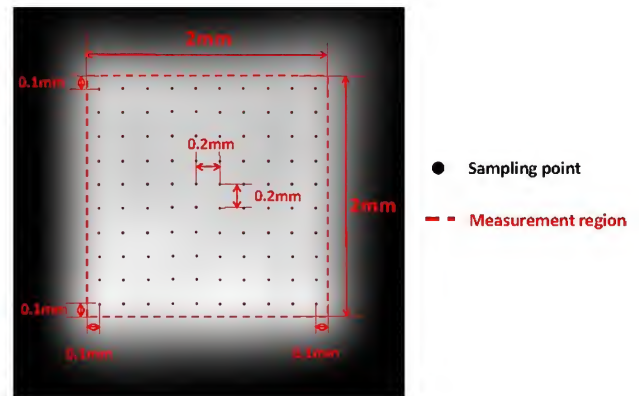


Fig. 5. Measurement points for the irradiance uniformity of light pattern.

due to more scattering rays generated around the tips of the Fresnel surface of F-BSFL.

### 3. Fabrication and Tolerance Analysis

The prototypes of both BSFL and F-BSFL were fabricated by CNC machining [Figs. 9(a) and 9(b)]. Limited by the accuracy of CNC machine, the pitch of each concentric circular notch in F-BSFL is larger than 1 mm and the depth of each concentric circular notch is 0.13 mm. To confirm their performances, a uniform flat-top He-Ne laser beam, instead of

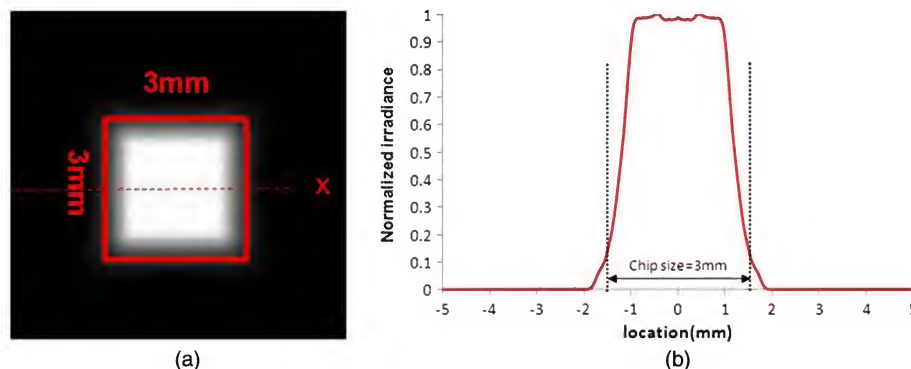


Fig. 4. (a) Simulated light pattern on the solar cell is square. (b) Irradiance distribution of the light pattern along  $x$  axis.

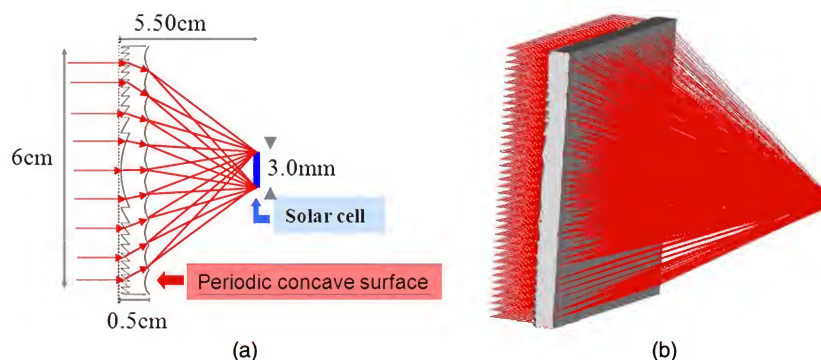


Fig. 6. (a) Schematic layout of F-BSFL and its optical path drawn. (b) 3D layout and rays distribution of F-BSFL drawn by ASAP software. A square light pattern on the solar cell can also be observed.

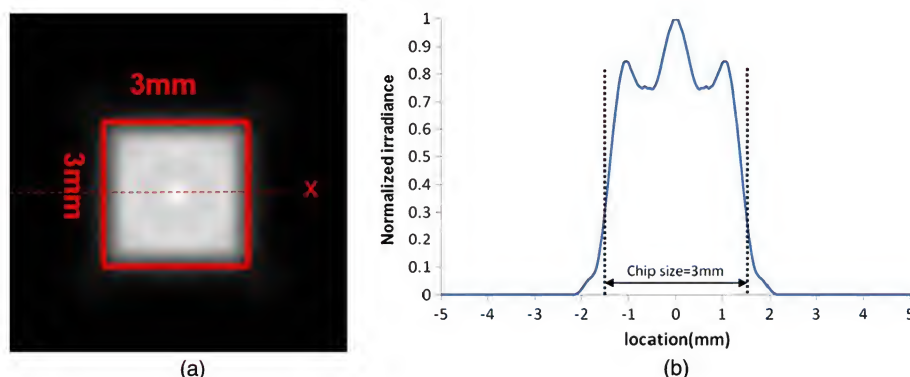


Fig. 7. (a) Simulated light pattern from F-BSFL on the solar cell is square. (b) Irradiance distribution of the light pattern along  $x$  axis.

Table 2. Simulated and Experimental Performances of BSFL and F-BSFL

Types	BSFL (Simulation)	BSFL (Measurement)	F-BSFL (Simulation)	F-BSFL (Measurement)
Minimum normalized irradiance	21%	N/A	30%	N/A
Chip size ( $\text{mm}^2$ )	$3.0 \times 3.0$	$3.0 \times 3.0$	$3.0 \times 3.0$	$3.0 \times 3.0$
TE	91%	76%	92%	82%
CE	84%	46%	69%	53%
CR	$314\times$	$314\times$	$400\times$	$400\times$
U (%)	22.55	N/A	57.69	N/A

sunlight and an integrating sphere, is utilized in measurement (Fig. 10). The light patterns at the focal plane formed by BSFL and F-BSFL are, respectively, shown in Figs. 11(a) and 11(b). The measured

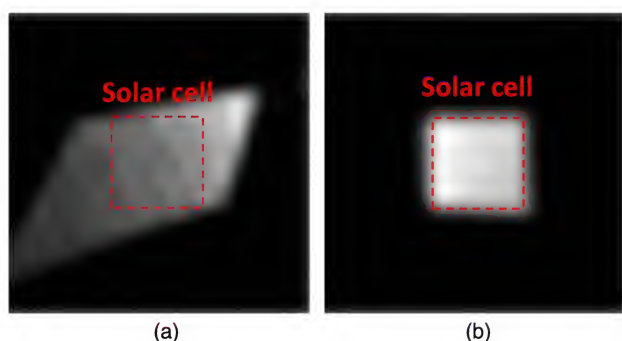


Fig. 8. Light patterns on the solar cell from different concave surfaces are distorted differently. (a) Outer concave surface generates a more distorted pattern. (b) Inner concave surface generates a less distorted one.

CE values and transmission efficiencies of BSFL and F-BSFL are also listed in Table 2. The deviation between the simulated and the measured values is mainly caused by the curvature radius error and high roughness on each periodic concave surface introduced in cutting the plastic lens using CNC machining. The minimum normalized irradiance and uniformity of experimental data are not shown in Table 2, which is judged zero in both BSFL and F-BSFL by observing Fig. 11. Some shadows are also visible in the pattern of F-BSFL. Besides F-BSFL's pattern is elongated in  $Y$  direction, which is introduced by the eccentricity in machining the first surface. This is due to several issues. For example, the spot images of Fig. 11 were captured by a camera, and overexposure forced the data of pixels with low irradiance to be automatically reduced to zero. Besides, a tool able to measure each irradiance of 100 sampling points within  $3 \text{ mm} \times 3 \text{ mm}$  is not currently available. Therefore, the simulation data of the uniformity is listed for reference. Compared with

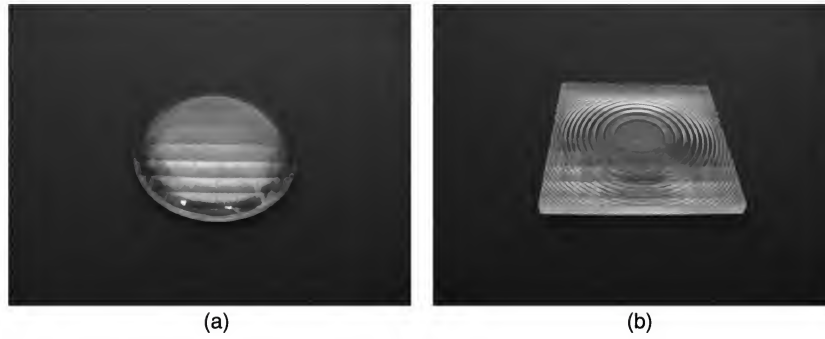


Fig. 9. Prototypes of (a) BSFL and (b) F-BSFL.

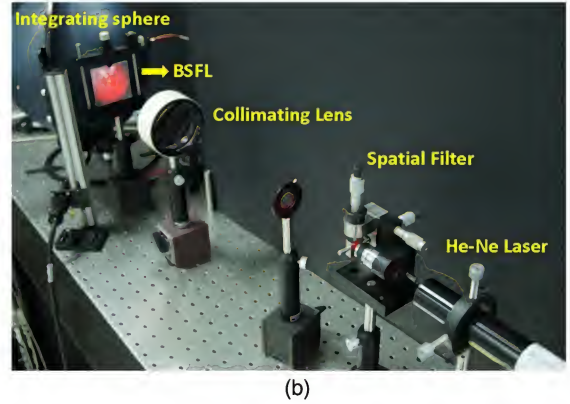
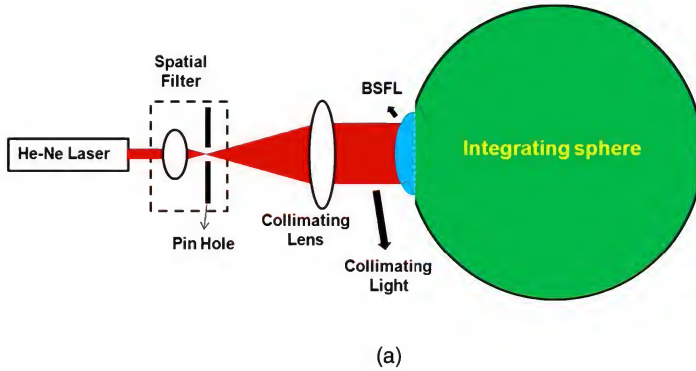


Fig. 10. Transmission efficiency measurement of the BSFL. (a) Optical setup and (b) experimental setup.

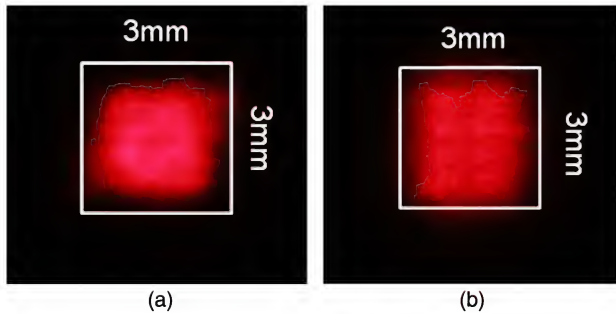


Fig. 11. Captured light patterns of (a) BSFL and (b) F-BSFL.

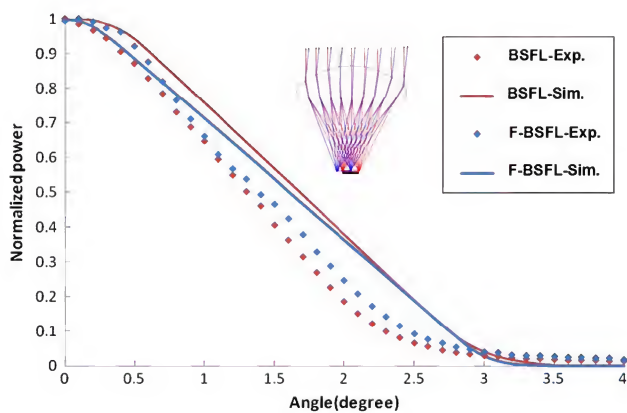


Fig. 12. Angular tolerance analysis and measurement results of the incident rays' angles into BSFL and F-BSFL.

a previous similar design by Ryu *et al.* [36], their simulated collection efficiencies of the  $9 \times 9$  array and the  $11 \times 11$  array are around 62% and 55%, respectively. Our current  $10 \times 10$  array design has a better performance. The simulated collection efficiencies of BSFL and F-BSFL are around 84% and 69%, respectively.

To evaluate the optical performance precisely, a full fabrication and assembly tolerance analysis is necessary. Using the half-width at half-maximum (HWHM) values in the solar cell, a sensitivity tolerance analysis was performed to identify the issues of the system. When we chose to ignore lens fabrication tolerances and focused only on assembly errors, we found that for both cases, the worst offenders were the slant angles of incident sunlight. In Fig. 12, for the BSFL, the HWHM values in simulation and experiments are about  $\pm 1.75^\circ$  and  $\pm 1.3^\circ$ , respectively. For the F-BSFL the values are  $\pm 1.6^\circ$  and  $\pm 1.45^\circ$ , respectively. Among other worst offenders, the degradation factors of BSFL's optical performance include the decentering and rotation of the solar cell and the rotation of the collection lens of BSFL, as illustrated in Fig. 13. The tolerance data, including measurement and simulation, are summarized in Table 3. The high-tolerance budget angular sensitivity much larger than  $0.1^\circ$  and positional sensitivity much larger than 0.1 mm, show that both BSFL and F-BSFL are feasible at a reasonable cost.



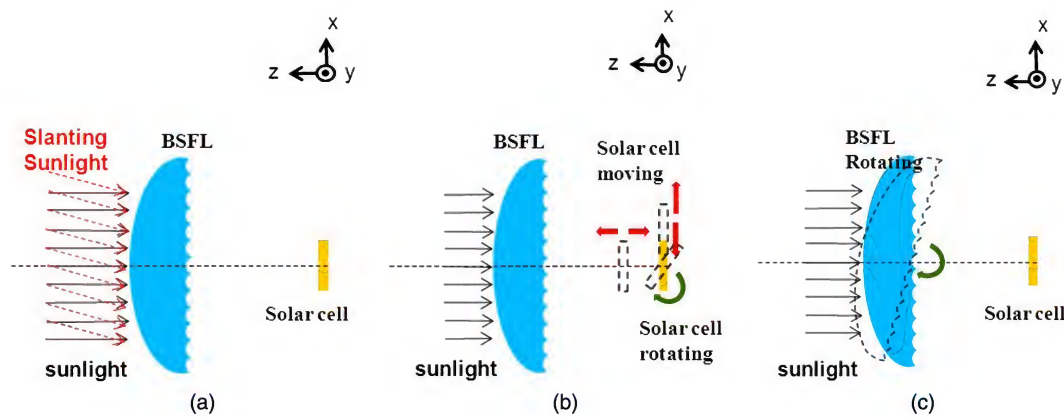


Fig. 13. Main degradation factors of BSFL's optical performance, including (a) slant of incident sunlight, (b) decentering and rotation of the solar cell, and (c) rotation of the collection lens of BSFL.

Table 3. Assembly Tolerance of BSFL and F-BSFL

Symbol	Tolerance	HWHM Values of Simulation Results (BSFL)	HWHM Values of Experimental Results (BSFL)	HWHM Values Simulation Results (F-BSFL)	HWHM Values Experimental Results (F-BSFL)
AS	Angular sensitivity of the CPV system with different incident light angle	$\pm 1.75^\circ$	$\pm 1.3^\circ$	$\pm 1.6^\circ$	$\pm 1.45^\circ$
ATMX	Assembling tolerance of CPV system by moving the solar cell along the $x$ axis	$\pm 1.5$ mm	$\pm 1.25$ mm	$\pm 1.55$ mm	$\pm 1.1$ mm
ATMZ	Assembling tolerance of CPV system by moving the solar cell along the $z$ axis	+4 mm to -3.5 mm	+6 mm to -5 mm	+4.5 mm to -5 mm	+7 mm to -6.5 mm
ATRSY	Angular tolerance by rotating the solar cell around the $y$ axis	$\pm 66^\circ$	$\pm 53^\circ$	$\pm 62^\circ$	$\pm 50^\circ$
ATRY	Assembling tolerance of BSFL rotating around the $y$ axis	$\pm 7.5^\circ$	$\pm 7.5^\circ$	$\pm 15^\circ$	$\pm 18^\circ$

#### 4. Conclusions

In this paper we have designed a BSFL and an F-BSFL to converge incident rays and shape these rays into a square spot for improving utilization efficiency of solar cell. The BSFL is composed of an aspheric front surface, an array of concave surfaces, and a solar cell. The F-BSFL has a similar structure except for using a Fresnel surface to replace the aspheric surface for reducing weight and volume. The final size of the square focal point in both designs is less than  $3 \text{ mm} \times 3 \text{ mm}$ . The transmission efficiency, the concentration ratio, the collection efficiency, and the light pattern's irradiance uniformity of BSFL and F-BSFL are 91% and 92%,  $314\times$  and  $400\times$ , 84% and 69%, and 22.55% and 57.69%, respectively. Both prototypes were fabricated using CNC machining. Their measured transmission and collection efficiencies are 76% and 46% for BSFL, and 82% and 53% for F-BSFL, respectively. In addition, the tolerance analysis in assembly shows that BSFL and F-BSFL are highly feasible and have potential to increase the optical utilization factor in most CPV systems.

The authors would like to thank Chi-Hung Lee for his helpful suggestions. This research was supported

partially by grants from the National Science Council, Taiwan, under contract numbers NSC100-2221-E-035-061, NSC101-2221-E-035-071, and NSC100-2632-E-035-001-MY3.

#### References

1. S. Kurtz and J. Geisz, "Multijunction solar cells for conversion of concentrated sunlight to electricity," *Opt. Express* **18**, A73–A78 (2010).
2. R. Winston, "Principles of solar concentrators of a novel design," *Sol. Eng.* **16**, 89–95 (1974).
3. K. Araki, T. Yano, and Y. Kuroda, "30 kW concentrator photovoltaic system using dome-shaped Fresnel lenses," *Opt. Express* **18**, A53–A63 (2010).
4. M. Park, K. Oh, J. Kim, H. W. Shin, and B. D. Oh, "A tapered dielectric waveguide solar concentrator for a compound semiconductor photovoltaic cell," *Opt. Express* **18**, 1777–1787 (2010).
5. J. M. Gordon, "Aplanatic optics for solar concentration," *Opt. Express* **18**, A41–A52 (2010).
6. J. H. Karp, E. J. Tremblay, and J. E. Ford, "Planar micro-optic solar concentrator," *Opt. Express* **18**, 1122–1133 (2010).
7. C. M. Wang, H. I. Huang, J. W. Pan, H. Z. Kuo, H. F. Hong, H. Y. Shin, and J. Y. Chang, "Single stage transmission type broadband solar concentrator," *Opt. Express* **18**, A118–A125 (2010).
8. N. Shatz, J. Bortz, and R. Winston, "Thermodynamic efficiency of solar concentrators," *Opt. Express* **18**, A5–A16 (2010).
9. C. G. Young, "A sun-pumped cw one-watt laser," *Appl. Opt.* **5**, 993–998 (1966).

10. A. Segal, M. Epstein, and A. Yogeve, "Hybrid concentrated photovoltaic and thermal power conversion at different spectral bands," *Sol. Eng.* **76**, 591–601 (2004).
11. R. Winston and J. M. Gordon, "Planar concentrators near the étendue limit," *Opt. Lett.* **30**, 2617–2619 (2005).
12. K. K. Chong, F. L. Siaw, C. W. Wong, and G. S. Wong, "Design and construction of non-imaging planar concentrator for concentrator photovoltaic system," *Rew. Eng.* **34**, 1364–1370 (2009).
13. C. F. Chen, C. H. Lin, H. T. Jan, and Y. L. Yang, "Design of a solar concentrator combining paraboloidal and hyperbolic mirrors using ray tracing method," *Opt. Commun.* **282**, 360–366 (2009).
14. D. Chemisana, "Building integrated concentrating photovoltaics : a review," *Renew. Sustain. Energ. Rev.* **15**, 603–611 (2011).
15. P. A. Davies, "Light-trapping lenses for solar cells," *Appl. Opt.* **31**, 6021–6026 (1992).
16. M. Victoria, C. Domínguez, I. Antón, and G. Sala, "Comparative analysis of different secondary optical elements for aspheric primary lenses," *Opt. Express* **17**, 6487–6492 (2009).
17. P. Benítez, J. C. Miñano, P. Zamora, R. Mohedano, A. Cvetkovic, M. Buljan, J. Chaves, and M. Hernández, "High performance Fresnel-based photovoltaic concentrator," *Opt. Express* **18**, A25–A40 (2010).
18. M. Hernandez, A. Cvetkovic, P. Benitez, and J. C. Miñano, "High-performance Kohler concentrators with uniform irradiance on solar cell," *Proc. SPIE* **7059**, 705908 (2008).
19. D. Esparza and I. Moreno, "Solar concentrator with diffuser segments," *Proc. SPIE* **8011**, 80117B (2011).
20. E. M. Kritchman, A. A. Friesem, and G. Yekutieli, "Efficient Fresnel lens for solar concentration," *Sol. Eng.* **22**, 119–123 (1979).
21. N. C. Yeh, "Analysis of spectrum distribution and optical losses under Fresnel lenses," *Renew. Sustain. Energ. Rev.* **14**, 2926–2935 (2010).
22. H. Zhai, Y. J. Dai, J. Y. Wu, R. Z. Wang, and L. Y. Zhang, "Experimental investigation and analysis on a concentrating solar collector using linear Fresnel lens," *Energy Convers. Manage.* **51**, 48–55 (2010).
23. D. Chemisana and M. Ibáñez, "Linear Fresnel concentrators for building integrated applications," *Energy Convers. Manage.* **51**, 1476–1480 (2010).
24. V. D. Rumyantsev, "Solar concentrator modules with silicone-on-glass Fresnel lens panels and multijunction cells," *Opt. Express* **18**, A17–A24 (2010).
25. X. Deng, X. Liang, Z. Chen, W. Yu, and R. Ma, "Uniform illumination of large targets using a lens array," *Appl. Opt.* **25**, 377–381 (1986).
26. Y. Lin, G. N. Lawrence, and J. Buck, "Characterization of excimer lasers for application to lenslet array homogenizers," *Appl. Opt.* **40**, 1931–1941 (2001).
27. A. Büttner and U. D. Zeitner, "Wave optical analysis of light-emitting diode beam shaping using microlens arrays," *Opt. Eng.* **41**, 2393–2401 (2002).
28. J. A. Hoffnagle and C. M. Jefferson, "Beam shaping with a plano-aspheric lens pair," *Opt. Eng.* **42**, 3090–3099 (2003).
29. T. R. M. Sales, "Structured microlens arrays for beam shaping," *Proc. SPIE* **5175**, 109–120 (2003).
30. T. R. M. Sales, "Structured microlens arrays for beam shaping," *Opt. Eng.* **42**, 3084–3085 (2003).
31. S. I. Chang, J. B. Yoon, H. Kim, J. J. Kim, B. K. Lee, and D. H. Shin, "Microlens array diffuser for a light-emitting diode backlight system," *Opt. Lett.* **31**, 3016–3018 (2006).
32. J. J. Yang, Y. S. Liao, and C. F. Chen, "Fabrication of long hexagonal micro-lens array by applying gray-scale lithography in micro-replication process," *Opt. Commun.* **270**, 433–440 (2007).
33. O. Homburg, A. Bayer, T. Mitra, J. Meinschien, and L. Aschke, "Beam shaping of high power diode lasers benefits from asymmetrical refractive micro-lens arrays," *Proc. SPIE* **6876**, 68760 (2008).
34. T. Bizjak, O. Homburg, A. Bayer, T. Mitra, and L. Aschke, "Free form micro-optics enable uniform off-axis illumination and superposition of high power laser devices," *Proc. SPIE* **7062**, 70620T (2008).
35. D. Hauschild, O. Homburg, T. Mitra, M. Ivanenko, M. Jarczyński, J. Meinschien, A. Bayer, and V. Lissotschenko, "Optimizing laser beam profiles using micro-lens arrays for efficient material processing: applications to solar cells," *Proc. SPIE* **7202**, 72020U (2009).
36. K. Ryu, J. G. Rhee, K. M. Park, and J. Kim, "Concept and design of modular Fresnel lenses for concentration solar PV system," *Sol. Eng.* **80**, 1580–1587 (2006).
37. W. J. Smith, *Modern Optical Engineering* (McGraw-Hill, 1976).
38. A. Büttner and U. D. Zeitner, "Wave optical analysis of light-emitting diode beam shaping using microlens arrays," *Opt. Eng.* **41**, 2393–2401 (2002).
39. O. Homburg, A. Bayer, T. Mitra, J. Meinschien, and L. Aschke, "Beam shaping of high power diode lasers benefits from asymmetrical refractive micro-lens arrays," *Proc. SPIE* **6876**, 68760B (2008).
40. T. Bizjak, O. Homburg, A. Bayer, T. Mitra, and L. Aschke, "Free form micro-optics enable uniform off-axis illumination and superposition of high power laser devices," *Proc. SPIE* **7062**, 70620T (2008).
41. D. Hauschild, O. Homburg, T. Mitra, M. Ivanenko, M. Jarczyński, J. Meinschien, A. Bayer, and V. Lissotschenko, "Optimizing laser beam profiles using micro-lens arrays for efficient material processing: applications to solar cells," *Proc. SPIE* **7202**, 72020U (2009).